Yilan crater, China: Evidence for an origin by meteorite impact

Ming CHEN [1,2]*, Christian KOEBERL [3], Dayong TAN[2,4], Ping DING[1,2], Wansheng XIAO[2,4],
Ning WANG[1,2], Yiwei CHEN[1,2], and Xiande XIE[2,4]

[1]State Key Laboratory of Isotope Geochemistry, Guangzhou Institute of Geochemistry, Chinese Academy of Sciences,
Guangzhou 510640, China
[2]CAS Center for Excellence in Deep Earth Science, Guangzhou 510640, China
[3]Department of Lithospheric Research, University of Vienna, Althanstrasse 14, Vienna A-1090, Austria
[4]Key Laboratory of Mineralogy and Metallogeny, Guangzhou Institute of Geochemistry, Chinese Academy of Sciences,
Guangzhou 510640, China
*Corresponding author. E-mail: mchen@gig.ac.cn

Abstract–The Yilan crater is 1.85 km in diameter and is located in the northeast of China's Heilongjiang Province. The crater is exposed in the Early Jurassic granite of the regional Paleozoic–Mesozoic granite complexes. The southern third of the crater rim is missing, but other rim sections are well preserved, with a maximum elevation above the present crater floor of 150 m. A drillcore from the center of the structure shows that the crater fill consists of 110 m thick lacustrine sediments underlain by a 319 m thick brecciated granite unit mainly composed of unconsolidated granite clasts and fragments. Melt products derived from the target granite, which include melted (and recrystallized) granite clasts, vesicular glass, and teardrop-shaped glass, were found in the brecciated granite unit at 218–237 m depth. Petrographic investigations of unmelted granite clasts in the brecciated granite unit from this depth interval show the presence of multiple sets of planar deformation features (PDFs) in quartz. Orientation measurements for 79 PDF sets in 38 quartz grains with a U-stage indicate the dominance of the $\omega\{10\bar{1}3\}$ and $\pi\{10\bar{1}2\}$ orientations with a relative frequency of 39% and 18%, respectively. Only 7.6% of the observed PDFs remain unindexed. The observations of PDFs with the appropriate orientations are clear evidence of shock metamorphism and thus of an impact origin of the Yilan structure. Crystallite aggregates of coesite embedded in silica glass were found in the impact-melted granite clasts. The carbon-14 dates of possibly impact-produced charcoal and lacustrine sediments from the crater fill suggest a young age for the impact event of 0.0493 ± 0.0032 Ma.

INTRODUCTION

China is a country with a vast territory. So far, only one relatively small impact structure has been confirmed in China, namely the Xiuyan crater (Chen et al. 2011; Schmieder and Kring 2020; Planetary and Space Science Center 2021). Recently, another circular geological structure in northeast China was brought to our attention in the course of an investigation of potential impact craters within China. The structure is centered 19 km northwest of the town of Yilan, Yilan County, Heilongjiang Province, and is located in the hilly area of the southeastern margin of the Lesser Xing'an Range.

The Lesser Xing'an Range is one of the best-preserved forest areas in China, and most of this area is covered by dense forests and crops. The structure has been known by local people for a long time as "Quanshan," a Chinese expression that is used to describe a circular mountain ridge. The origin of the structure has not been investigated before. The shape of the structure had attracted our attention for further studies.

Well-defined diagnostic criteria related to shock metamorphism have been established for the identification and confirmation of terrestrial impact structures because complex geological processes on Earth obstruct the impact record (e.g., Reimold 2007;

French and Koeberl 2010; Reimold et al. 2014). Typical evidence of shock metamorphism in rocks and minerals may include shatter cones, planar deformation features (PDFs) in minerals, diaplectic mineral glasses, and shock-produced high-pressure mineral phases (e.g., Dietz 1959; Chao 1967; Stöffler and Langenhorst 1994; Grieve et al. 1996; French 1998; Koeberl 2002; Wieland et al. 2006; Ferrière et al. 2009; French and Koeberl 2010; Langenhorst and Deutsch 2012; Reimold et al. 2014). In the study of the Yilan crater, we have focused our investigation on possible shock metamorphic effects of rocks and minerals of the structure. A geological drilling project was carried out on the crater floor to explore the structure and to collect rock samples for analysis.

GEOLOGICAL SETTING

The Yilan crater is located in the south-central part of Heilongjiang province at latitude and longitude of 46°23′03″N and 129°18′50″E, respectively (Fig. 1a). Heilongjiang province is situated in the eastern part of the Central Asian Orogenic Belt (Wang et al. 2017; Ge et al. 2018; Song et al. 2018). The Central Asian Orogenic Belt extends from the Urals in the west, through Kazakhstan, northwestern China, Mongolia, and northeastern China, to the Okhotsk Sea in the Russian Far East (Windley et al. 2007; Zhou et al. 2009). A large north–south trending granitic belt, the Lesser Xing'an Range, covers an extensive area in the Heilongjiang province, which is characterized by voluminous Paleozoic–Mesozoic granitoids, with relatively few Paleozoic strata intercalated with the granitoids (Fig. 2a; Meng et al. 2011; Wu et al. 2011). The granitoids mainly consist of alkali feldspar granite, monzogranite, and granodiorite (Dong et al. 2017; Zhu et al. 2017; Ge et al. 2019). The Yilan structure is exposed in Early Jurassic granite of the Lesser Xing'an Range granitoids (Fig. 2b). The bedrock of the crater is formed of alkali feldspar granite. Paleozoic strata found in the area of the Lesser Xing'an Range include Devonian sandstone and conglomerate, as well as Carboniferous and Permian tuff (Institute of Geology Chinese Academy of Geological Sciences 2016). Both the Paleozoic volcano-sedimentary strata and the granitoids are locally and unconformably covered by Cretaceous sandstone and Quaternary deposits.

The Yilan crater, with a rim-to-rim diameter of 1.85 km, displays an almost continuous concentric ridge, with a wide gap in the south (Figs. 1b and 1c). The missing part of the rim of the apparent crater structure is about 2 km in extension. Although part of the crater rim is missing, other sections of the crater rim are well preserved. The crater shows a raised ridge above the surrounding surface. The maximum rim elevation above the present crater floor is 150 m, and the rim crest is 110–150 m above the surrounding area. The inner slope of the crater rim is between 25° and 35°, and the outer slope of the crater rim is between 10° and 25°. The elevation at the center of the crater is about 170 m above sea level.

The surface of the crater rim is mostly covered with a thin layer of soils and forests. In addition, granite fragments and boulders of up to 2 m in size have been observed locally on the rim crest and the slopes (Fig. 3). All the fragments and blocks observed on the rim are of the same granite type (alkali feldspar granite) with a pink color. Most of these fragments and boulders of granite on the outcrops are relatively fresh or weakly weathered. The central depression of the crater is about 1.1 km in diameter, and is now covered with swamp and forest wetland, with thick sequences of lacustrine sediments.

SAMPLES AND METHODS

A core was drilled to explore the structure and to collect subsurface samples for our study. The geographic coordinates of the borehole are 46°22′54″N and 129°18′57″E, which is 400 m to the southeast of the structure's center. The borehole penetrated through the crater fill (the lacustrine deposits in the upper part and the brecciated granite unit in the lower part) into granite basement and reached a final depth of 438 m. The initial borehole diameter is 325 mm, and the final hole diameter is 110 mm. The drilling started in May 2020 and ended in August 2020. The cores are now preserved at the Guangzhou Institute of Geochemistry, Chinese Academy of Sciences.

Granite clasts, granite melt clasts, and large fragments of granite from drill cores were used to explore the possible presence of shock metamorphic features. A total of 120 thin sections were prepared from the samples, 85 of which were made from granite clasts (ranging from 0.05 to 3 mm in size) from 218 to 237 m depth, thin sections from granite melt clasts from 218 to 237 m, and 30 thin sections from large fragments of granite (ranging from 5 to 10 cm in size) from 110 to 114 m, as well as 142 to 143.5 m depth. All these thin sections were studied with an optical petrologic microscope.

A total of 38 grains of PDF-bearing quartz in 20 thin sections were used for measurements of crystallographic orientations of PDFs. The quartz grains were investigated using a 4-axis universal stage (U-stage). The c-axis and the poles to all sets of PDFs were plotted on a stereographic Wulff net. Crystallographic orientations of PDFs were indexed
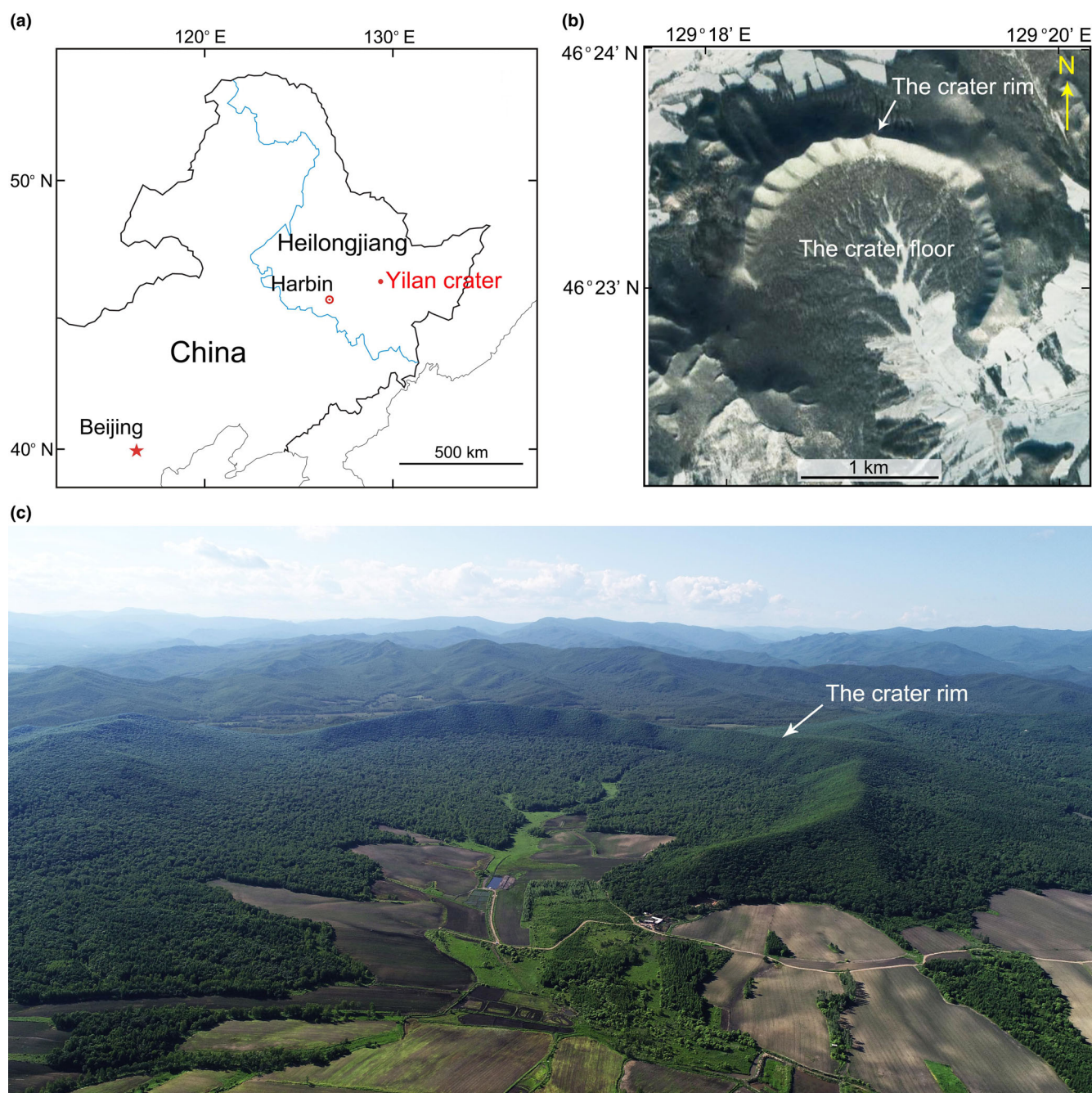
Fig. 1. Location and overview of the Yilan crater. a) Location map of the Yilan crater. The crater is located in the south-central part of the Heilongjiang province. b) A satellite image of the Yilan crater, showing the crater rim with a wide gap in the south and a circular depression on the crater floor (taken on December 2013) from Google Earth. c) A panoramic view from the southeast outside the crater, taken by an unmanned aerial vehicle on June 2019 at an altitude of 500 m above the ground. The star in Figure 1 is used here to mark the capital city of China. (Color figure can be viewed at wileyonlinelibrary.com.)

using the stereographic projection template displaying the possible pole orientations of common sets of PDFs within a 5-degree envelope of measurement error, using the methods described by Ferrière et al. (2009).

Raman spectroscopic analyses were carried out at the Guangzhou Institute of Geochemistry (GIG) with a confocal Raman microscope (Renishaw, RM-2000) at 532 nm excitation wavelength. The instrument was calibrated using the 520 cm^{-1} line of a silicon wafer. Signal accumulations lasted for 120 s.

X-ray diffraction patterns of samples were recorded with a Rigaku D-max Rapid-V micro-diffractometer
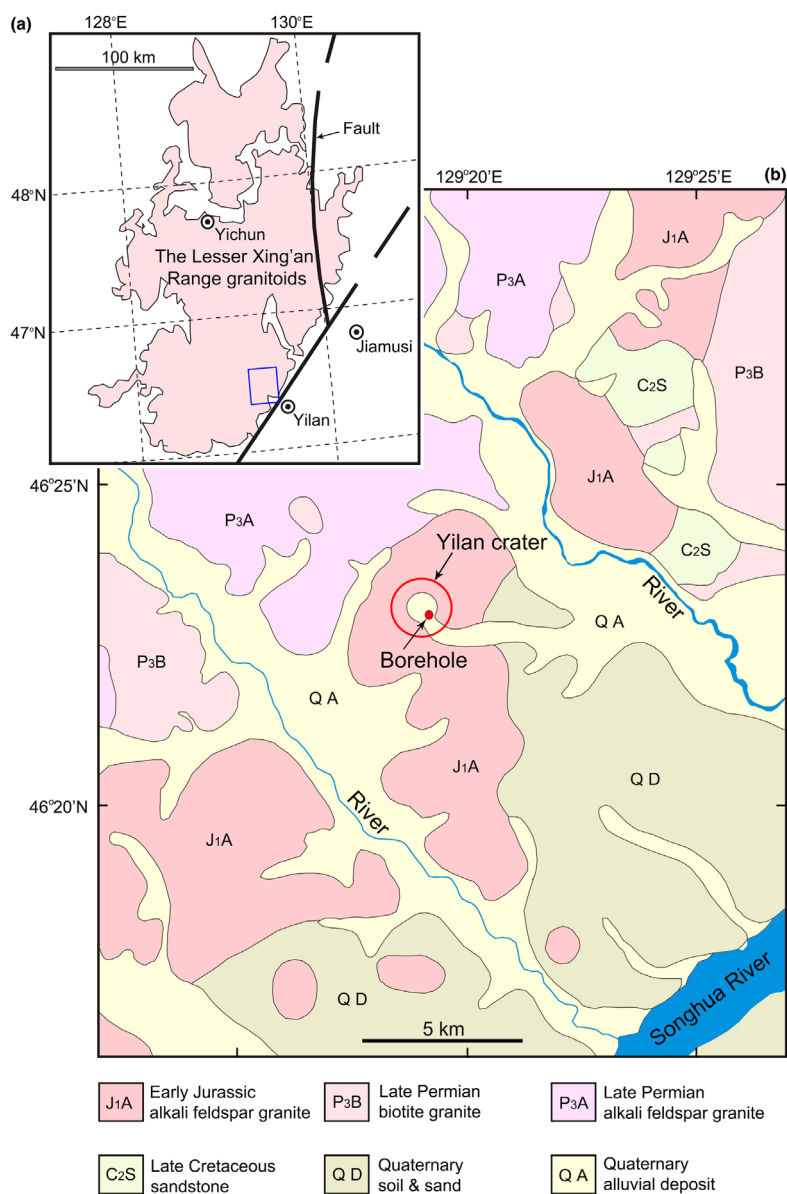
Fig. 2. a) Sketch map showing the distribution of the Lesser Xing'an Range granitoids in northeastern China (modified from Ge et al. 2018). The blue rectangular frame in the lower part of the inset figure indicates the area of (b). b) Geological sketch map of the Yilan crater and its surrounding area (modified from Heilongjiang Geological Bureau 1972; Institute of Geology Chinese Academy of Geological Sciences 2016). Note the location of the borehole. (Color figure can be viewed at wileyonlinelibrary.com.)

(μ-XRD), also at GIG, which is equipped with a microfocus rotating anode source (MicroMax-007HFM X-ray generator) and a curved imaging plate detector. The diffractometer was operated with Cu-Kα radiation (λ = 0.15418 nm) generated at 40 kV and 30 mA. A built-in CCD camera was used to select the measurement areas. The μ-XRD data were collected in transmission mode using a 0.1 mm collimator and a collection time of 100 s. The data were collected as two-dimensional images and then converted into 2θ-intensity profiles using the Rigaku 2DP software. For each XRD pattern the interpretable 2θ region was selected manually.

The chemical compositions of minerals and silicate glasses were determined using a Cameca SXFive FE Electron Probe Microanalyzer at GIG. The compositions of quartz (eight analyses), K-feldspar (10 analyses), and albite (10 analyses) were determined on minerals in the thin sections prepared from granite fragments in the drill core at 142 m depth (Table 1).

Fig. 3. Outcrops of granite along the rim. a) The crest of the northern rim. b) The inner wall of the eastern rim. (Color figure can be viewed at wileyonlinelibrary.com.)

The compositions of silicate glass (5 analyses), feldspar glass (10 analyses) and granite glass (13 analyses) were determined on the thin sections prepared from clasts in the drill core at 225 m depth (Table 1). Operating conditions of 15 kV accelerating voltage and 20 nA beam current were used in the course of this study. A

Table 1. Chemical compositions of quartz, coesite, silica glass, K-feldspar, albite, feldspar glass, granite glass, and granite from the Yilan crater (wt%).

	Quartz		Coesite		Silica glass		K-feldspar		Albite		Feldspar glass		Granite glass		Granite	
	(8)	STDEV	(8)	STDEV	(5)	STDEV	(10)	STDEV	(10)	STDEV	(10)	STDEV	(13)	STDEV	(4)	STDEV
SiO_2	100.25	0.60	98.94	0.81	99.04	0.94	64.16	0.54	68.19	0.93	65.65	1.03	75.95	0.64	75.82	0.12
TiO_2	b.d.l.		b.d.l.		b.d.l.		b.d.l.		b.d.l.		b.d.l.		0.08		0.07	0.01
Al_2O_3	0.02	0.02	b.d.l.		0.05	0.05	18.60	0.13	20.03	0.24	18.94	0.39	13.18	0.21	12.21	0.71
FeO	b.d.l.		b.d.l.		0.02	0.02	0.14	0.10	0.22	0.17	0.21	0.24	1.45	0.05	1.24	0.21
MnO	b.d.l.		b.d.l.		b.d.l.		b.d.l.		b.d.l.		b.d.l.		0.06	0.02	0.03	0.02
MgO	b.d.l.		b.d.l.		b.d.l.		b.d.l.		b.d.l.		b.d.l.		0.18	0.04	0.12	0.09
CaO	b.d.l.		b.d.l.		0.02	0.02	b.d.l.		0.31	0.16	0.08	0.08	0.37	0.15	0.43	0.08
Na_2O	b.d.l.		b.d.l.		b.d.l.		0.20	0.04	11.34	0.22	4.21	1.23	3.62	0.10	3.86	0.35
K_2O	b.d.l.		b.d.l.		b.d.l.		16.34	0.11	0.11	0.04	9.04	1.66	4.50	0.16	4.72	0.15
P_2O_5	b.d.l.		b.d.l.		b.d.l.		b.d.l.		b.d.l.		b.d.l.		b.d.l.	0.02	0.02	0.01
Total	100.27		98.94		99.13		99.44		100.20		98.13		99.39		98.52	

Numbers in parentheses are the number of analyses. The compositions of quartz, coesite, silica glass, K-feldspar, albite, feldspar glass, and granite glass were analyzed by electron microprobe. The composition of bulk granite was analyzed by X-ray fluorescence spectrometry (for sample information, see text for details).
STDEV = standard deviations of analyses; b.d.l. = below detection limit.

peak counting time of 180 s was chosen based on the intensity of characteristic X-ray lines and desired precision for the element contents.

Whole-rock major element abundances of the bulk granite were determined using a Rigaku ZSX Primus IV X-ray fluorescence spectrometer at GIG (Table 1). The X-ray fluorescence (XRF) analytical methods follow those reported by Goto and Tatsumi (1994). Among the four analyzed granite samples, two of them are from granite fragments in the drill cores at 142 and 430 m depth, respectively, whereas the other two are from the crater rim. The rocks were crushed and ground in an agate ring mill, and the resulting powder was used for analyses of major elements. The abundances of major elements were determined by analyses of glass disks with a 1:8 sample to $Li_2B_4O_7$ flux ratio. A pre-ignition method was used to determine the loss on ignition prior to major element analyses. The granite standards GBW07103 and GBW07125 were used as external standards (GBW 2021). The accuracies of the XRF analyses are estimated to be about 1% (relative) for SiO_2, 2% relative for other major oxides present in concentrations greater than 0.5 wt% and 5% (relative) for MnO and P_2O_5, respectively.

The carbon-14 dating method was used to derive possible age constraints on the impact event. Fragments of charcoal were handpicked from the core samples of the brecciated granite unit between 218 and 237 m depth. One sample of charcoal was used for radiocarbon dating. Also, two samples of silty clay sediments collected from the core samples of lacustrine deposits at depths of 109.5 and 102.5 m were used for radiocarbon dating. The samples were first treated with a standard acid–base–acid protocol to remove carbonates and humic/organic acid contaminants and rinsed. After having been freeze-dried, the sample was placed into a quartz tube, with silver wool and clean CuO needles, and then baked at 350 °C in an oven to further eliminate modern carbon contaminants. Then the tube was vacuumed, sealed, and heated at 850 °C in an oven for 2 h to oxidize organic carbon to CO_2. The CO_2 gas was purified and finally graphitized, using the method proposed by Xu et al. (2007). The amounts of carbon used for graphitization ranged from 0.83 to 0.85 mg. Two coal samples with 0.86 and 0.93 mg of carbon were treated as blank measurements in the same way as mentioned above. The sample preparation was carried out at the State Key Laboratory of Isotopic Geochemistry in Guangzhou, China, and the graphite target was measured by accelerator mass spectrometry with a precision of 0.3% at Peking University of China. The ^{14}C data were corrected for the stable carbon isotopic fractionation ($\delta^{13}C$) and calibrated by the

IntCal20 curve using the software Calib 8.2 (Stuiver et al. 2020).

RESULTS

Lithostratigraphy of the Drill Core

The drilling from the crater floor penetrated to a depth of 438 m and revealed that the crater fill has a thickness of 429 m (Fig. 4). The crater fill mainly consists of lacustrine sediments and unconsolidated granite clasts and fragments. The lacustrine sediments are 110 m thick and composed of muddy and silty-clay materials. This deposit is underlain by a brecciated granite unit between the depths of 110 and 429 m. Fractured bedrock or coarse blocks of granites occur below 429 m.

All the rock samples collected from the drill cores belong to the same kind of alkali feldspar granite. The granite in the brecciated granite unit is similar to that occurring at the crater rim, and no other rock type was encountered throughout the brecciated granite unit. The granite is mainly composed of quartz (25–30 vol%), K-feldspar (40–45 vol%), albite (20–25 vol%) and minor mica. The chemical analyses show that the granite has high silica (>75 wt% SiO_2) and alkali contents (>8 wt% Na_2O+K_2O) (Table 1).

The brecciated granite unit is mainly composed of angular granite clasts less than 2 cm in size, with minor amounts of large granite fragments up to 35 cm in size. The upper unit, from 110 to 218 m depth, is mainly composed of fine- to coarse-grained granite clasts of up to 2 cm in size. The large granite fragments up to 35 cm in size are only present in the depth intervals from 110 to 114 m, and 142 to 143.5 m. In the depth interval from 218 to 237 m, a fine- to medium-grained granite clast layer was noted, in which the clasts are mostly less than 5 mm in size. The lower unit from 237 to 429 m depth consists of fine-grained granite clasts less than 3 mm in size. The angular clasts in the brecciated granite unit indicate that they were not transported very far, and most likely were deposited insitu or close from the source area, or came off the rim wall.

Abundant granite melts associated with unmelted granite clasts are found in the drill core samples of the brecciated granite unit at 218–237 m depth (Fig. 4; Table 2). The granite melts include granite melt clasts, vesicular glass, and teardrop-shaped glass particles (Fig. 5). The abundance of the granite melts in this depth interval is about 5–10 vol%.

The granite melt clasts are mainly composed of melted quartz and melted feldspar. The melted quartz occurs as irregular nodules, whereas the melted feldspar occurs as veinlets with flow textures (Fig. 6a). The

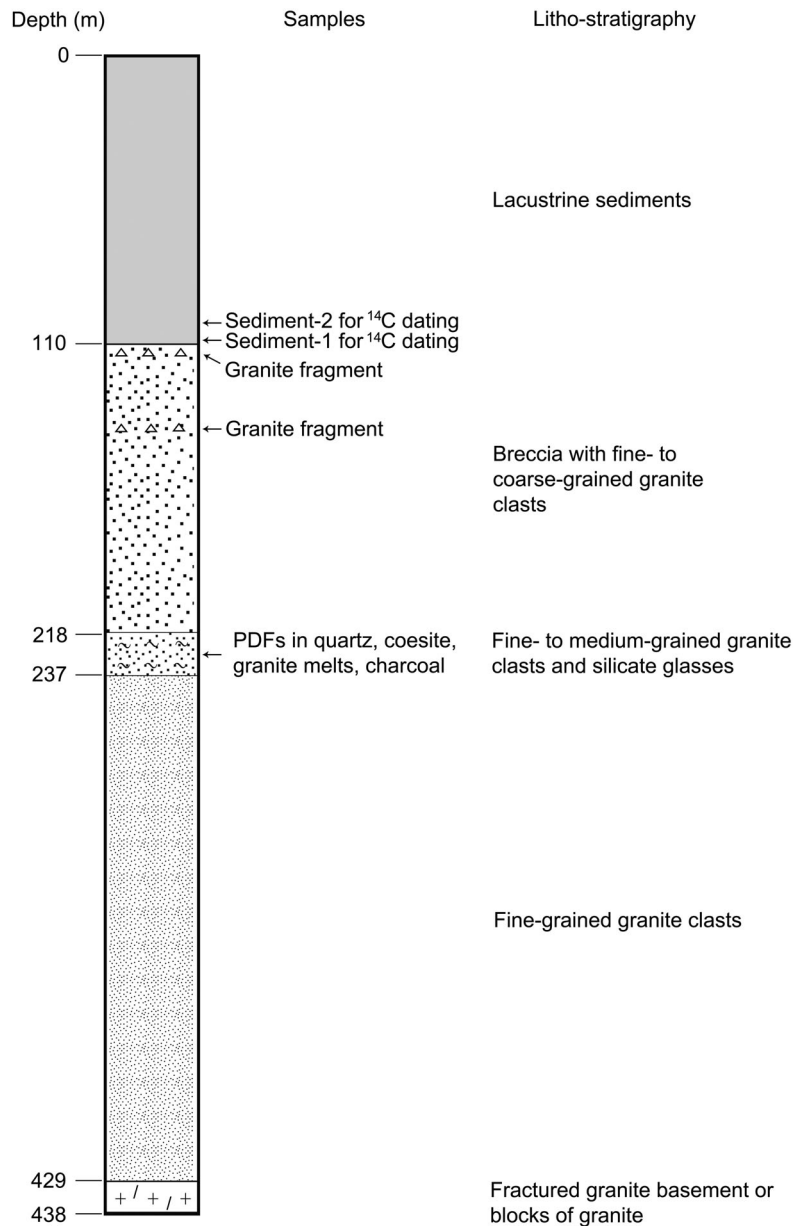Depth (m)   Samples   Litho-stratigraphy

Fig. 4. Schematic lithostratigraphy of the borehole into the floor of the Yilan crater. The crater fill consists of a thick layer of lacustrine sediments underlain by a brecciated granite unit. At the bottom of the borehole, fractured granitic basement was encountered.

Table 2. Shock metamorphic features of granite from the drill core samples of the Yilan crater.

Samples	Depths (m)	Granite melts	PDFs in quartz	Coesite
Large fragments	110–114	No	No	No
Large fragments	142–143.5	No	No	No
Fine-grained clasts	218–237	Abundant granite melts including granite melt clasts, vesicular glass, and teardrop-like glass	Abundant PDF-bearing grains; multiple sets of PDFs	Abundant coesite

Fig. 5. Teardrop-shaped glass particles occurring in the brecciated granite unit at 218–237 m depth. (Color figure can be viewed at wileyonlinelibrary.com.)
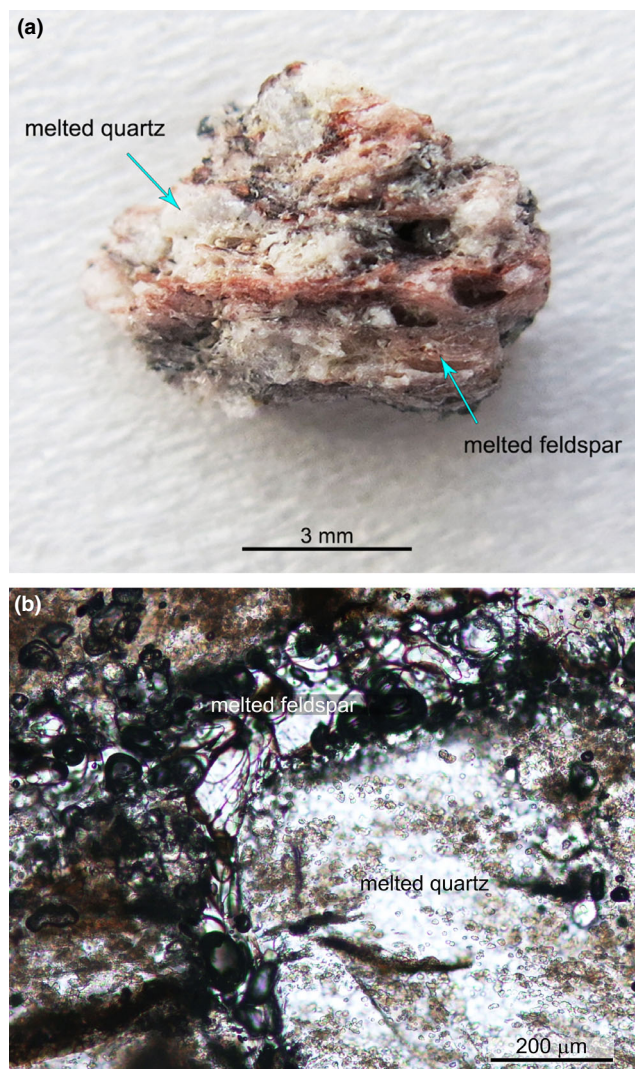

Fig. 6. A clast of partially melted granite from the brecciated granite unit at 225 m depth. a) The clast displays pink veinlets of melted feldspar with flow textures and milky-white melted quartz nodules in between the veinlets. b) Thin section photomicrograph of the granite melt clast plane-polarized light. The melted quartz is composed of silica glass and contains crystallite aggregates of coesite with light brown color; the melted feldspar is full of vesicles. (Color figure can be viewed at wileyonlinelibrary.com.)

melted quartz in the granite melt clasts is a mixture of silica glass and some tiny phases recrystallized from silica glass (Fig. 6b). The electron microprobe analyses show that the silica glass has an average composition of 99.04 wt% SiO_2, which is similar to the quartz (100.25 wt% SiO_2) in the bedrock granite of the crater (Table 1). The melted feldspar (feldspar glass), which contains on average 65.65 wt% SiO_2, 18.94 wt% Al_2O_3, 4.21 wt% Na_2O and 9.04 wt% K_2O, 0.08 wt% CaO, and 0.21 wt% FeO, has a composition between that of K-feldspar and albite, characterizing a mixed composition derived by melting of two feldspars (Table 1).

Figure 5 shows some teardrop-shaped glass particles. The particles are dark brown in color, variably transparent to translucent, and are 3–10 mm in size. The average composition of the glass particles is 75.95 wt% SiO_2, 0.08 wt% TiO_2, 13.18 wt% Al_2O_3, 1.45 wt% FeO, 0.06 wt% MnO, 0.18 wt% MgO, 0.37 wt% CaO, 3.62 wt% Na_2O, and 4.50 wt% K_2O, which is similar to the composition of the bulk granite (Table 1).

Several fragments of charcoal ranging from 3 mm to 1.5 cm in size, mixed together with unconsolidated granite clasts, were found in the brecciated granite unit at 218–237 m depth (Fig. 7a). The charcoal is hard, brittle, and displays dark color and semimetallic luster. Carbonized xylem vessel microstructures can be observed (Fig. 7b). Such xylem vessel microstructures in trees constitute a model natural microfluidic system (Capron et al. 2014). The preservation of xylem vessel microstructures characterizes a wood charcoal. The Raman spectrum of the charcoal is dominated by two intense bands at about 1588 and 1358 cm^{-1} (Fig. 7c), which can be assigned to the G band (graphite-like phase) and the D band (disordered phase) of charcoal, respectively (Cohen-Ofri et al. 2006; Francioso et al. 2011).

PDFs in Quartz

Quartz grains with PDFs were found in the granite clasts of the brecciated granite unit at 218–237 m depth (Fig. 4; Table 2). The distribution of PDF-bearing quartz grains in the granite clasts varies from one thin section to the other. Of the 85 thin sections that were prepared, 35 thin sections contain quartz grains displaying PDFs. The number of PDF sets and also their orientations vary among different grains of individual clasts within the same thin sections.

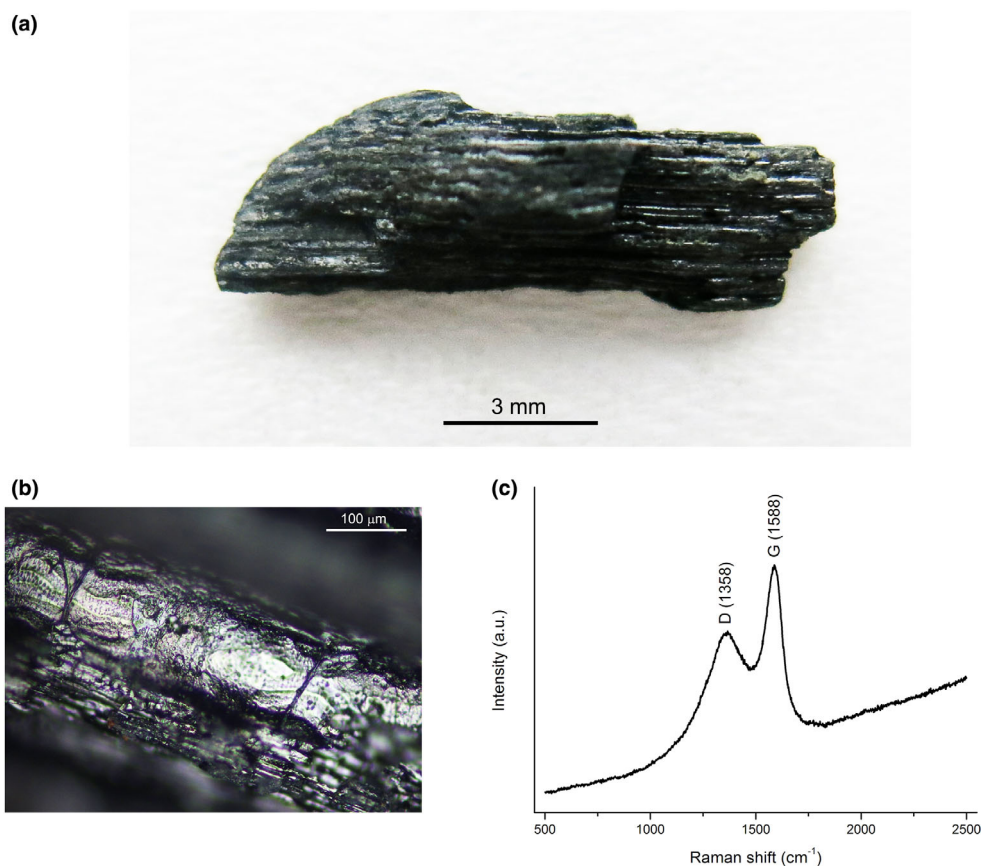**(a)**

(b)

(c)

Fig. 7. Charcoal recovered from the brecciated granite unit of 218–237 m depth. a) A charcoal fragment of dark color and semi-metallic luster. b) Xylem vessel microstructures preserved in charcoal. c) Raman spectrum of charcoal showing the G band of graphite-like phase and the D band of a disordered phase. (Color figure can be viewed at wileyonlinelibrary.com.)

The investigations of 20 thin sections from large fragments of granite at depths from 110 to 114 m and of 10 thin sections at depths from 142 to 143.5 m, respectively, found no PDFs in quartz. Apparently, the large fragments of granite were only weakly shocked.

Most quartz grains in the granite clasts contain multiple sets of PDFs (Fig. 8). The number of PDFs within each individual grain of quartz varies from one to four. The PDFs in quartz are sharp/narrow and straight. The apparent thickness of individual PDF lamellae is 1–2 μm, and the spacings between individual planes vary from 2 to 10 μm. A total of 79 sets of PDFs identified in 38 quartz grains within 20 thin sections have been measured to determine their crystallographic orientations. A histogram of angles between c-axis and poles to PDFs, binned to 5°, is shown in Fig. 9. Of the 79 measured sets in quartz grains, a total of 73 sets of PDFs (92.4%) corresponded to rational crystallographic orientations and thus could be indexed. Only six values (7.6%) remained unindexed. The indexed PDFs in quartz correspond to rational crystallographic orientations with Miller–Bravais indices of $e\{10\bar{1}4\}$,

$\omega\{10\bar{1}3\}$, $\pi\{10\bar{1}2\}$, $\xi\{11\bar{2}2\}$, r/z$\{10\bar{1}1\}$, s$\{11\bar{2}1\}$, $\rho\{21\bar{3}1\}$, x$\{51\bar{6}1\}$, and m/a $\{10\bar{1}0\}/\{11\bar{2}0\}$. The most abundant forms of PDFs in quartz are $\omega\{10\bar{1}3\}$ and $\pi\{10\bar{1}2\}$ with frequencies of 39.6% and 17.7%, respectively (Table 3). No PDFs parallel to the basal plane (0001) were observed in our data set.

The Presence of Coesite

The melted quartz in the granite melt clasts contains a number of crystallite aggregates with light brown color (Fig. 6b). These polycrystalline phases occur as granular, elongated, and irregular crystallite aggregates enclosed in silica glass (Fig. 10). The granular crystallite aggregates have sizes up to 25 μm, with individual crystal sizes in the crystallite aggregates less than 1 μm. The elongated crystallite aggregates are up to 50 μm in length and have a width up to 8 μm. Electron microprobe analyses show that the silica glass (99.04 wt% SiO_2) and the crystallite aggregates (98.94 wt% SiO_2) enclosed in the silica glass have compositions similar to that of the quartz (100.25 wt% $\pm$ 0.60 SiO_2) in the bedrock granite (Table 1).
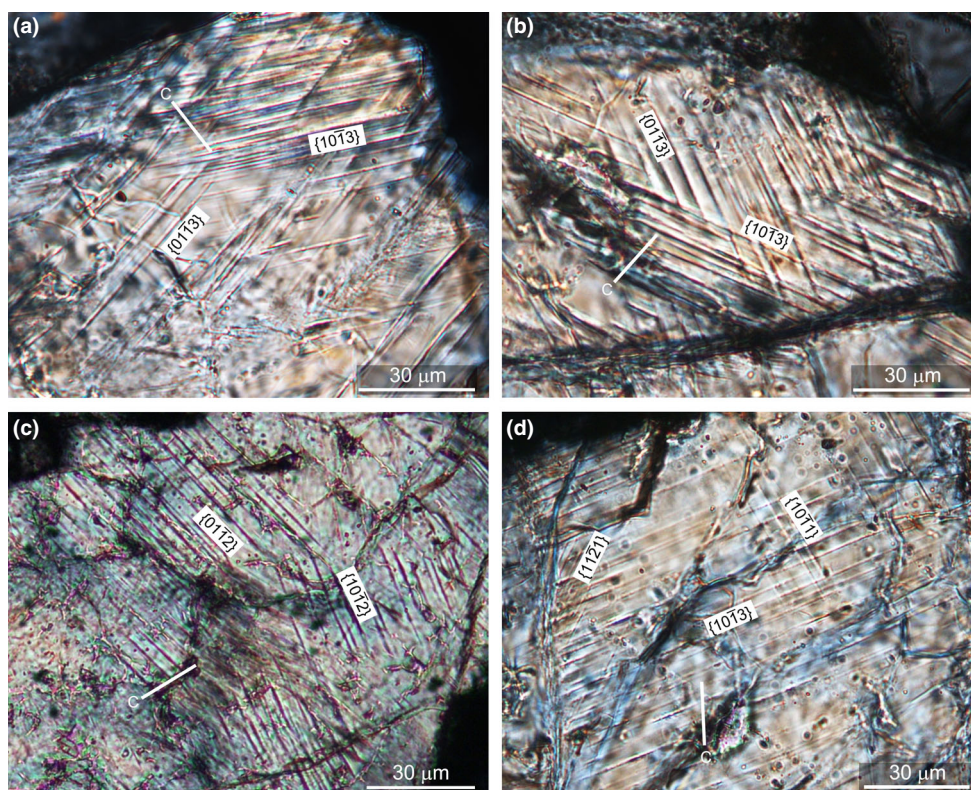
Fig. 8. Thin section photomicrographs of planar deformation features (PDFs) in quartz grains under cross-polarized light. The crystallographic orientations (Miller–Bravais indices) of the PDFs are marked on the images. The samples of fine-grained quartz and granite clasts are all from the brecciated granite unit at depths from 218 to 237 m. The quartz *c*-axis is indicated. (Color figure can be viewed at wileyonlinelibrary.com.)

Micro-Raman spectroscopy of the crystallite aggregates enclosed in silica glass show a strong peak at 520 cm^{-1} and some minor peaks at 815, 786, 466, 427, 356, 326, 268, 204, 174, and 150 cm^{-1} (Fig. 11). All these Raman peaks can be attributed to coesite (cf. Boyer et al. 1985; Hemley 1987; Jackson et al. 2016). The broad bands at 488 and 810 cm^{-1} are attributed to low-density silica glass (Okuno et al. 1999). Coesite is a high-pressure mineral and is known to crystallize from silica melt under pressure. The property of low-density silica glass demonstrates that the remaining silica melt was quenched after pressure release.

Micro X-ray diffraction analyses of melted quartz nodules confirmed the presence of coesite. The X-ray diffraction patterns show coesite, quartz, and amorphous silica glass (Fig. 12). More than 14 diffraction lines can be assigned to coesite. In the two-dimensional X-ray diffraction image, distinct diffraction rings from coesite show that the coesite occurs as crystallite aggregates. The X-ray diffraction patterns also display a broad amorphous feature, which appears as a broad band with the equivalent Bragg angle at $2\theta = 22°$, indicating the existence of amorphous silica (Abou Rida and Garb 2014).

Carbon-14 Age Dating

Three samples of charcoal and lacustrine sediments from the crater were radiocarbon-dated for this study.

Fraction modern (F_m) values of charcoal and coal (for the blank measurement) samples are 0.0071 ± 0.0002 (1σ, corresponding to a ^{14}C age of $39,740 \pm 180$ a BP) and 0.0041 ± 0.0002 (1σ, corresponding to a ^{14}C age of $44,220 \pm 390$ a BP), respectively, showing that the F_m values of charcoal are clearly beyond the 2σ (95.4%) confidence interval of laboratory background (Table 4). After the modern carbon contamination correction (background correction) and tree ring curve IntCal20 calibration, the age of the charcoal is derived at $49,230 \pm 3210$ cal BP (0.0493 ± 0.0032 Ma, or $47,280 \pm 3210$ cal BC). The large uncertainty of ±3210 years is mainly caused by the error propagation when the data are corrected for the modern carbon contamination. The newly published IntCal20 curve allows a range of up to 55 ka cal BP for radiocarbon calibration (Reimer et al. 2020). The age of the charcoal is within the range of radiocarbon calibration.

The lacustrine sediments in the borehole have a thickness of 110 m. Two samples of light-gray silty clay
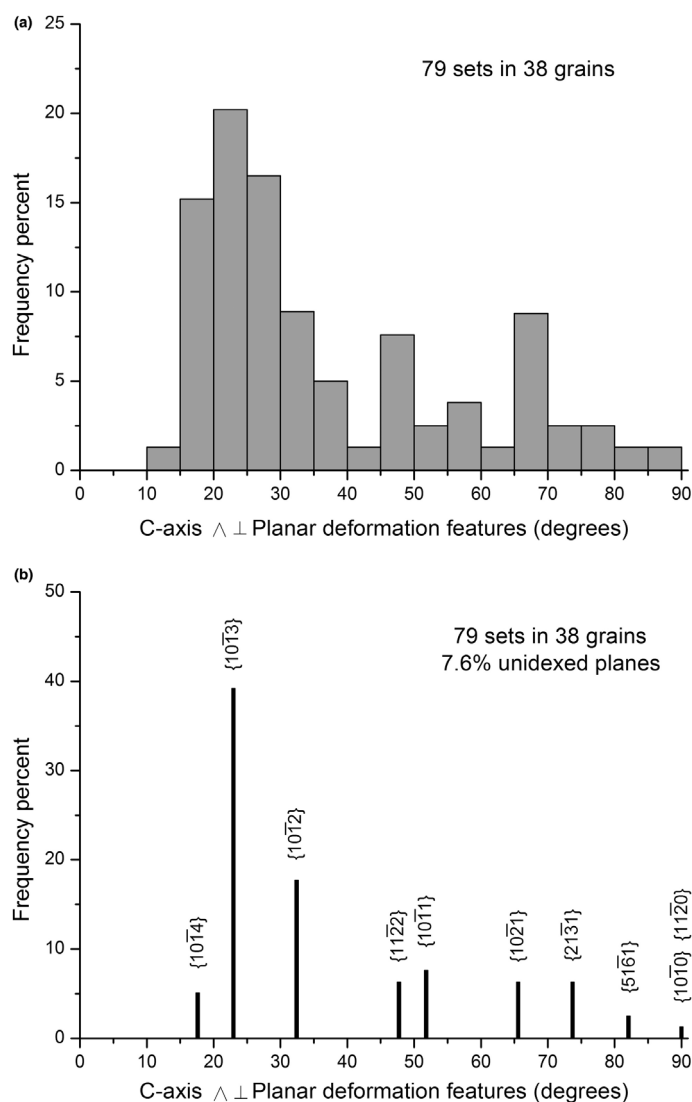
Fig. 9. Crystallographic orientations of planar deformation features in 38 quartz grains from the brecciated granite unit from 218 to 237 m depth. a) Frequency distributions of angles between *c*-axis and PDF planes, binned at 5°. b) Frequency distributions of indexed PDF orientations in quartz grains.

from core depths of 109.5 and 102.5 m, respectively, were radiocarbon-dated and yielded ages of 48,360 ± 3780 cal BP (0.0484 ± 0.0038 Ma, or 46,410 ± 3780 cal BC) and 44,010 ± 1700 cal BP (0.044 ± 0.0017 Ma, or 42,060 ± 1700 cal BC), respectively (Table 4). The ages of lacustrine sediments are younger than of charcoal occurring in the brecciated granite unit.

DISCUSSION

PDFs in Quartz

PDFs are the most prominent shock-induced deformation indicators that occur in many rock-forming silicates, especially in quartz and feldspars (Chao 1967; Engelhardt and Bertsch 1969; Stöffler and Langenhorst 1994; Grieve et al. 1996; French 1998). The occurrence of PDFs in quartz has been widely accepted as diagnostic evidence for shock metamorphism (e.g., Stöffler and Langenhorst 1994; Grieve et al. 1996; French 1998; French and Koeberl 2010; Langenhorst and Deutsch 2012). The finding of PDFs in quartz in the granite clasts in the crater fill of the Yilan crater provides unambiguous evidence of shock metamorphism of target rocks, and thus that the structure is of impact origin.

It has been well established that the most common orientations of PDF planes in quartz from impact craters are parallel to rhombohedral planes, such as the

Table 3. Planar deformation features and crystallographic indices in 38 quartz grains from the core drilled into the Yilan crater, using the stereographic projection template for the indexing (after Ferrière et al. 2009).

Planes and symbols	Miller–Bravais Indexes	Polar angle with *c*-axis	Number of PDFs	Percent
e	{10 $\bar{1}$ 4}	17.62°	4	5.1
ω	{10 $\bar{1}$ 3}	22.95°	31	39.2
π	{10 $\bar{1}$ 2}	32.42°	14	17.7
ξ	{11 $\bar{2}$ 2}	47.73°	5	6.3
r/z	{10 $\bar{1}$ 1}	51.79°	6	7.6
s	{11 $\bar{2}$ 1}	65.56°	5	6.3
ρ	{21 $\bar{3}$ 1}	73.71°	5	6.3
x	{51 $\bar{6}$ 1}	82.07°	2	2.6
m/a	{10 $\bar{1}$ 0},{11 $\bar{2}$ 0}	90.00°	1	1.3
Unindexed	–	–	6	7.6
Total	–	–	79	100

basal (0001), ω{10$\bar{1}$3}, and π{10$\bar{1}$2} (e.g., Stöffler and Langenhorst 1994; Grieve et al. 1996; Ferrière et al. 2009; Langenhorst and Deutsch 2012). The main forms of PDFs developed in the quartz grains of the granite clasts in the Yilan crater are found to be ω{10$\bar{1}$3} and π{10$\bar{1}$2}.

Shock waves radiating from the projectile target interface decline in peak pressure rapidly outward (French 1998). PDFs in quartz develop at shock pressures between 10 and 35 GPa (e.g., Stöffler and Langenhorst 1994; Grieve et al. 1996; French 1998). Measurements of PDF orientations in quartz from Canadian impact structures indicated that some impact craters show a dominant presence of the ω{10$\bar{1}$3} orientations, whereas others display high frequencies of both ω{10$\bar{1}$3} and π{10$\bar{1}$2} (Robertson et al. 1968). Recent investigations also showed that PDFs in quartz in meta-grywacke clasts from the polymict lithic breccia of the Bosumtwi crater in Ghana (10.5 km in diameter) had dominant ω{10$\bar{1}$3} orientations (Ferrière et al. 2009). The shocked gneiss in the polymict breccia of the Xiuyan crater, 1.8 km in diameter, displays high frequencies of both the ω{10$\bar{1}$3} and π{10$\bar{1}$2} orientations (Chen et al. 2010). It is well established that the orientation of PDFs in quartz is related to the shock stage or shock degrees of the rocks (e.g., Stöffler and Langenhorst 1994). The presence of ω{10$\bar{1}$3} requires a shock pressure >10 GPa, whereas the presence of π{10$\bar{1}$2} requires a shock pressure >20 GPa (Grieve et al. 1996; French 1998). The dominant occurrence of ω{10$\bar{1}$3}, with only few π{10$\bar{1}$2} orientations, in the PDF-bearing quartz at the Yilan crater shows that the granite clasts were weakly to moderately shocked. The absence of PDFs
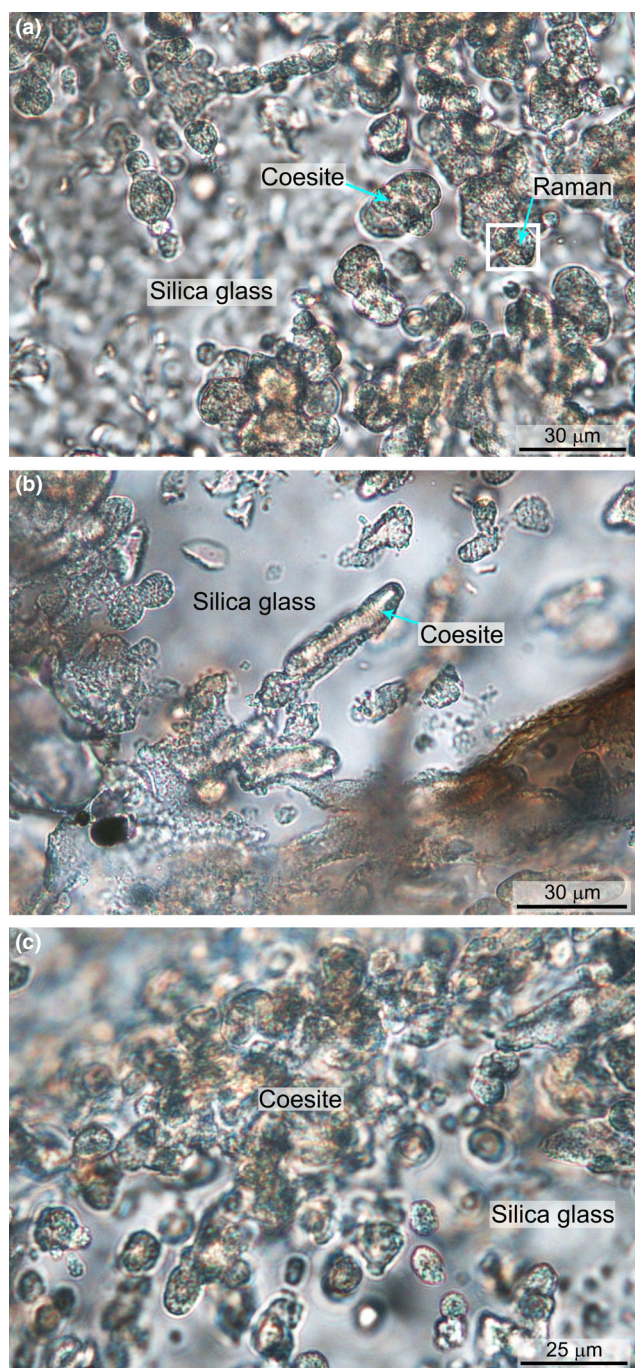

Fig. 10. Crystallite aggregates of coesite embedded in silica glass in granite melt clasts, which occur in the brecciated granite unit at depths from 218 to 237 m, plane-polarized light. a) Granular crystallite aggregates of coesite enclosed in silica glass. The white rectangle shows the area for Raman analysis. b) Elongated crystallite aggregates of coesite enclosed in silica glass. c) Irregular crystallite aggregates of coesite. (Color figure can be viewed at wileyonlinelibrary.com.)

parallel to the basal plane (0001) in the analyzed samples could be due to the elevated shock level of the samples or the limited number of analyses. The existence of PDFs
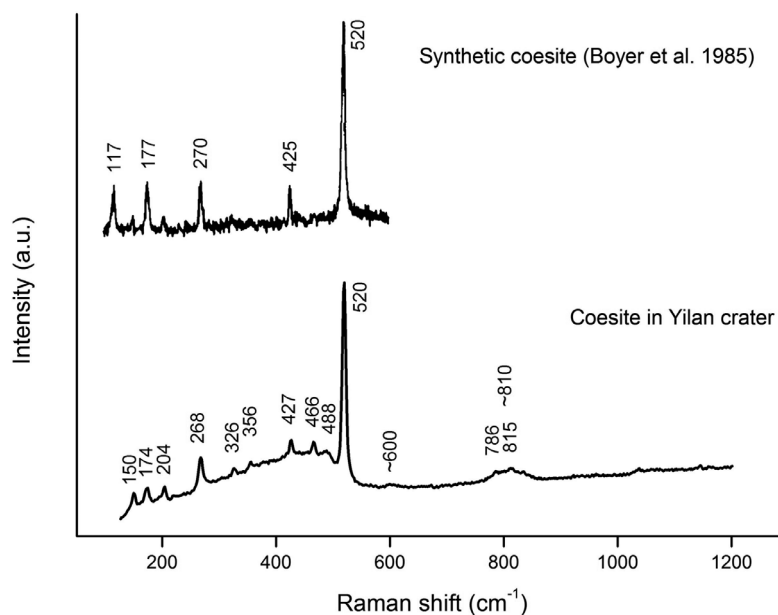
Fig. 11. Raman spectrum of coesite associated with silica glass, which was measured at the marked area on Fig. 8a. Raman peaks at 815, 786, 520, 466, 427, 356, 326, 268, 204, 174, and 150 cm^{-1} are attributed to coesite, whereas the broad bands from 250 to 550 cm^{-1} and at about 488, 600, and 810 cm^{-1} correspond to silica glass. The inserted spectrum of synthetic coesite is from Boyer et al. (1985).

parallel to the (0001) plane commonly corresponds to a shock pressure less than 10 GPa (Grieve et al. 1996). The analyzed samples of this study could be more strongly shocked. The large granite fragments in the core, which contain no PDFs in quartz, could be debris off the crater rim.

Shock-Induced Coesite

Coesite is a high-pressure modification of silica (Chao et al. 1960). One of the most critical characteristics of shock-induced coesite, in comparison with coesite from deep Earth settings, is that the shock-induced coesite is intimately associated with silica glass (Chao 1967; Stöffler and Langenhorst 1994). The impact-induced transformation of quartz to coesite requires a peak shock pressure between 30 and 60 GPa (Stöffler and Langenhorst 1994; Grieve et al. 1996). Several mechanisms have been proposed for the formation of coesite from shocked quartz, for example, by crystallization from silica melt (Langenhorst 2003; Chen et al. 2010; Langenhorst and Deutsch 2012; Fazio et al. 2017; Jaret et al. 2017), the subsolidus nucleation from diaplectic silica glass (Chao 1967; Stöffler and Langenhorst 1994; Stähle et al. 2008) and the direct subsolidus transformation from quartz (Folco et al. 2018).

Coesite in the Yilan crater occurs in melted quartz within the granite melt clasts of the brecciated granite

unit. The existence of both the melted quartz and the melted feldspar in the granite melt clasts indicates partial impact melting of the granite (Fig. 6; Table 1). The crystallite aggregates of coesite embedded in silica glass in the melted quartz indicate a rapid crystallization of coesite from the silica melt. The shock-induced coesite in terrestrial impact craters commonly occurs as crystallite aggregates of coesite associated with silica glass, and individual crystal sizes of coesite are generally less than 1 μm in size (Stöffler and Langenhorst 1994; Chen et al. 2010; Jaret et al. 2017; Folco et al. 2018; Yin et al. 2019). The occurrence and features of coesite in the Yilan crater are similar to those observed in other terrestrial impact craters; for example, a number of crystallite aggregates of coesite embedded in silica glass were found in the shock-metamorphosed gneiss within the impact-produced polymict breccia of the Xiuyan crater (Chen et al. 2010, 2013). Crystallite aggregates of coesite embedded in silica glass were also found in the silica amygdules of the target basalt of the Lonar crater (Jaret et al. 2017). The granular and elongated crystallite aggregates of coesite from Yilan, Xiuyan, and Lonar craters indicate crystallization of coesite from shock-produced silica melt from quartz (Chen et al. 2010, 2013; Jaret et al. 2017).

A Simple Crater

On Earth, impact craters with diameters of less than about 4 km (in crystalline rocks) have generally
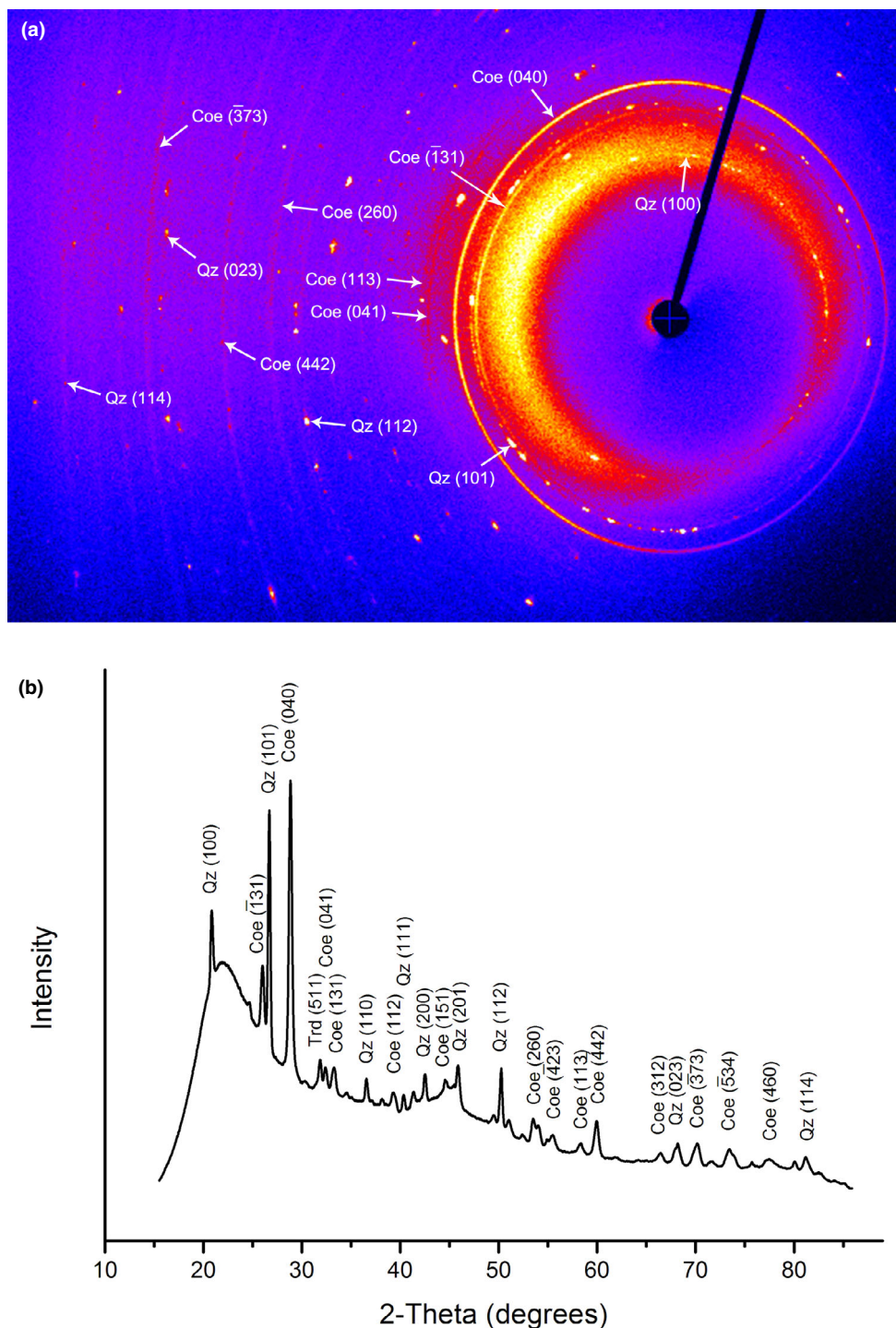
Fig. 12. X-ray diffraction pattern obtained from a melted quartz nodule in a granite melt clast of the breccia at 225 m depth. a) The two-dimensional X-ray diffraction image shows diffraction rings and diffraction spots that can be indexed to coesite (Coe) and quartz (Qz), respectively. b) The 2θ-intensity profile of this X-ray diffraction pattern converted from the two-dimensional X-ray diffraction image. (Color figure can be viewed at wileyonlinelibrary.com.)

the topographic form of so-called "simple" (or bowl-shaped) craters (e.g. French 1998). The Yilan structure, which formed in granitic basement rocks, has a rim-to-

rim diameter of 1.85 km. The depth from the maximum rim elevation to the present crater floor is 150 m. The rim crest is 110–150 m above the surrounding area. The

Table 4. Results of radiocarbon dating of charcoal and lacustrine sediments from the Yilan crater.

Samples	Lab code	C size (mg)	Depth (m)	^{14}C age (a BP, ±1σ)	F_m (±1σ)	^{14}Cage* (a BP, ±1σ)	Calibrated age (cal BC, ±1σ)
Charcoal	GZ9225	0.85	220	39,740 ± 180	0.0071 ± 0.0002	46,870 ± 3850	47,280 ± 3210
Sediment-1	GZ9369	0.83	109.5	37,560 ± 190	0.0093 ± 0.0002	45,380 ± 4530	46,410 ± 3780
Sediment-2	GZ9368	0.85	102.5	35,470 ± 170	0.0121 ± 0.0003	40,710 ± 2530	42,060 ± 1700
Coal-1[†]	GZ9231	0.86	–	44,220 ± 390	0.0041 ± 0.0002	–	–
Coal-2[†]	GZ9137	0.93	–	44,190 ± 220	0.0041 ± 0.0001	–	–

*^{14}C age with background correction.
[†]Background; Lab, laboratory; F_m, fraction modern; BP, before present; BC, before Christ; cal, calibrated.

drilling into the crater floor revealed that the crater fill composed of the lacustrine sediments in the upper part and the brecciated granite in the lower part have a combined thickness of 429 m (Fig. 4).

The presence of lacustrine sediments 110 m in thickness demonstrates that a lake developed in the crater after the formation of the impact structure, and that the crater should have had a complete rim in its early stage. Although part of the crater rim is missing, the rim in the northern part of the crater is well preserved. The cause for the missing part of the rim in the southern segment of the crater remains under investigation.

Fallback Ejecta

The chemical compositions of teardrop-shaped glass particles in the brecciated granite unit at depths between 218 and 237 m are similar to that of the bedrock granite of the crater (Table 1). This indicates that the glasses formed by impact-induced bulk melting of target granite. The presence of teardrop-shaped glass particles in the crater fill provides evidence for the presence of fallback ejecta (e.g., Settle 1980). Such teardrop-shaped glass particles are usually known as splash forms (compare, e.g., the occurrences at Bosumtwi; Koeberl et al. 2007). The occurrence of granite-derived melt particles, together with intact granite clasts in the crater fill of the Yilan crater, is similar to fallback ejecta described from other crater structures (e.g., Meteor Crater, Kring 2017). A series of strongly shock-metamorphosed rocks and minerals in the brecciated granite unit, as indicated by the presence of melted granite, coesite, and PDFs in quartz, occur together with the fallback materials. It is an interesting phenomenon that the fallback ejecta occur in the middle of the breccated granite unit in the crater fill. The occurrence of the fallback ejecta and the relation to the cratering mechanism needs further investigation.

Possible Age of Impact Event

Charcoal fragments occur together with granite clasts in the brecciated granite unit, indicating that both the charcoal and the granite clasts were deposited coevally. Therefore, the charcoal could have been formed during the impact event. The carbon-14 dating of charcoal gave an age of 0.0493 ± 0.0032 Ma. The age of the charcoal provides a possible age constraint for the impact event.

Charcoal associated with impact cratering has rarely been reported. Schultz et al. (2014) found residues of plant materials in alleged impact-melt breccia of Pampean strata of Argentina, where the morphological and chemical biosignatures of plant matter had been preserved. Charcoal was also reported in the proximal ejecta of the Kaali craters (Losiak et al. 2016). Charcoal is a product of wood burning in an oxygen-poor atmosphere. As the temperature increases, the major structural components of the wood break down while water, CO, CO_2, and other gases are released, which results in the formation of charcoal (Cohen-Ofri et al. 2006). Forest trees on the target surface could have been destroyed during the impact. A minor amount of tree residue could have been instantly turned into charcoal in the ejecta at the impact-induced high temperature, and partially fell back into the crater fill as fallback ejecta. As we have seen, the charcoal was found in the same depth interval in the brecciated granite unit at 218–237 m depth as the teardrop-shaped glass particles. The charcoal occurs nearly in the middle of the brecciated granite unit. Any later geological event cannot deposit the charcoal at the position where it was found. The impact-heated rock debris may also result in the carbonization of wood fragments enclosed in these materials (Losiak et al. 2016). The finding of charcoal in the Yilan crater is a rare occurrence where charcoal has been preserved in a brecciated granite unit of the crater fill.

The impact-brecciated granite unit is overlain by lacustrine sediments. The lacustrine sediment samples for the carbon-14 dating were collected from the bottom of the lacustrine sediment sequence, which was deposited after the formation of the impact crater. The carbon-14 dating of lacustrine sediments at 109.5 and 102.5 m depth resulted in ages of 0.0484 ± 0.0038 Ma and 0.044 ± 0.0017 Ma, respectively. The ages of the lacustrine sediments are slightly younger than the age of the charcoal from the brecciated granite unit. Therefore, the age of charcoal $(0.0493 \pm 0.0032$ Ma) may correspond to the time when the meteorite impact took place. However, future research is necessary to further investigate the significance of these ages.

CONCLUSIONS

The Yilan crater is an impact structure with a diameter of 1.85 km and a current rim elevation of up to 150 m above the present-day crater floor. The crater was formed in granitic bedrock. The crater fill consists of lacustrine sediments 110 m thick that are underlain by an impact-brecciated granite unit of 319 m thickness. The existence of PDFs in quartz, as well as crystallite aggregates of coesite enclosed in silica glass, in the granite clasts of the brecciated granite unit provides clear evidence for an impact origin of the structure. The carbon-14 datings of charcoal and lacustrine sediments from the crater fill indicate that the impact event took place at 0.0493 ± 0.0032 Ma ago.

REFERENCES

Abou Rida M. and Harb F. 2014. Synthesis and characterization of amorphous silica nanoparticles from aqueous silicates using cationic surfactants. *Journal of Metals, Materials and Minerals* 24:37–42.

Boyer H., Smith D. C., Chopin C., and Lasnier B. 1985. Raman microprobe (RMP) determinations of natural and synthetic coesite. *Physics and Chemistry of Minerals* 12:45–48.

Capron M., Tordjeman P. H., Charru F., Badel E., and Cochard H. 2014. Gas flow in plant microfluidic networks controlled by capillary valves. *Physical Review E* 89:033019.

Chao E. C. T. 1967. Shock effects in certain rock-forming minerals. *Science* 156:192–202.

Chao E. C. T., Shoemaker E. M., and Madsen B. M. 1960. First natural occurrence of coesite. *Science* 132:220–222.

Chen M., Xiao W., and Xie X. 2010. Coesite and quartz characteristic of crystallization from shock-produced silica melt in the Xiuyan crater. *Earth and Planetary Science Letters* 297:306–314.

Chen M., Koeberl C., Xiao W., Xie X., and Tan D. 2011. Planar deformation features in quartz from impact-produced polymict breccia of the Xiuyan crater, China. *Meteoritics & Planetary Science* 46:729–736.

Chen M., Yin F., Li X., Xie X., Xiao W., and Tan D. 2013. Natural occurrence of reidite in the Xiuyan crater of China. *Meteoritics & Planetary Science* 48:796–805.

Cohen-Ofri I., Weiner L., Boaretto E., Mintz G., and Weiner S. 2006. Modern and fossil charcoal: Aspects of structure and diagenesis. *Journal of Archaeological Science* 33:428–439.

Dietz R. S. 1959. Shatter cones in cryptoexplosion structures (meteorite impact?). *Journal of Geology* 67:496–505.

Dong Y., Ge W. C., Yang H., Bi J. H., Wang Z. H., and Xu W. L. 2017. Permian tectonic evolution of the Mudanjiang Ocean: Evidence from zircon U-Pb-Hf isotopes and geochemistry of a NS trending granitoid belt in the Jiamusi Massif, NE China. *Gondwana Research* 49:147–163.

Engelhardt W. von and Bertsch W. 1969. Shock-induced planar deformation structures in quartz from the Ries crater, Germany. *Contributions to Mineralogy and Petrology* 20:203–234.

Fazio A., Mansfeld U., and Langenhorst F. 2017. Coesite in suevite from the Ries impact structure (Germany): From formation to post-shock evolution. *Meteoritics & Planetary Science* 52:1437–1448.

Ferrière L., Morrow J. R., Amgaa T., and Koeberl C. 2009. Systematic study of universal-stage measurements of planar deformation features in shocked quartz: Implications for statistical significance and representation of results. *Meteoritics & Planetary Science* 44:925–940.

Folco L., Mugnaioli E., Gemelli M., Masotta M., and Campanale F. 2018. Direct quartz-coesite transformation

in shocked porous sandstone from Kamil Crater (Egypt). *Geology* 46:739–742.

Francioso O., Sanchez-Cortes S., Bonora S., Roldán M. L., and Certini G. 2011. Structural characterization of charcoal size-fractions from a burnt *Pinus pinea* forest by FT-IR, Raman and surface-enhanced Raman spectroscopies. *Journal of Molecular Structure* 994:155–162.

French B. M. 1998. Trace of catastrophe: A handbook of shock-metamorphic effects in terrestrial meteorite impact structure. LPI Contribution 954. Houston, Texas: Lunar and Planetary Institute. 120 p.

French B. M. and Koeberl C. 2010. The convincing identification of terrestrial meteorite impact structures: What works, what doesn't, and why. *Earth-Science Reviews* 98:123–170.

GBW. 2021. Reference materials web site of China. www.gbw365.com

Ge M., Zhang J., Li L., and Liu K. 2018. A Triassic-Jurassic westward scissor-like subduction history of the Mudanjiang Ocean and amalgamation of the Jiamusi Block in NE China: Constraints from whole-rock geochemistry and zircon U-Pb and Lu-Hf isotopes of the Lesser Xing'an-Zhangguangcai Range granitoids. *Lithos* 302–302:263–277.

Ge M., Zhang J., Li L., and Liu K. 2019. Ages and geochemistry of Early Jurassic granitoids in the Lesser Xing'an–Zhangguangcai Ranges, NE China: Petrogenesis and tectonic implications. *Lithosphere* 11:804–820.

Goto A. and Tatsumi Y. 1994. Quantitative analysis of rock samples by an X-ray fluorescence spectrometer (I). *The Rigaku Journal* 11:40–59.

Grieve R. A. F., Langenhorst F., and Stöffler D. 1996. Shock metamorphism of quartz in nature and experiment: II. Significance in geoscience. *Meteoritics & Planetary Science* 31:6–35.

Heilongjiang Geological Bureau. 1972. Yilan geological map (L-52-XVI, 1:200000). Harbing.

Hemley R. J. 1987. Pressure dependence of Raman spectra of SiO_2 polymorphs: A-quartz, coesite and stishovite. In *High-pressure research in mineral physics*, edited by Manghnani M. H. and Syono Y. Tokyo: Terra Scientific Publishing Co. pp. 347–359.

Institute of Geology Chinese Academy of Geological Sciences. 2016. *Geological map of China (1:1000000)*. Beijing: Geological Publishing House. pp. 221–224.

Jackson J. C., Horton J. W. Jr., Chou I. M., and Belkin H. E. 2016. Coesite in suevites from the Chesapeake Bay impact structure. *Meteoritics & Planetary Science* 51:946–965.

Jaret S. J., Phillips B. L., King D. T., Glotch T. D., Rahman Z., and Wright S. P. 2017. An unusual occurrence of coesite at the Lonar crater, India. *Meteoritics & Planetary Science* 52:147–163.

Koeberl C. 2002. Mineralogical and geochemical aspects of impact craters. *Mineralogical Magazine* 66:745–768.

Koeberl C., Brandstätter F., Glass B. P., Hecht L., Mader D., and Reimold W. U. 2007. Uppermost impact fallback layer in the Bosumtwi crater (Ghana): Mineralogy, geochemistry, and comparison with Ivory Coast tektites. *Meteoritics & Planetary Science* 42:709–729.

Kring D. A. 2017. *Guidebook to the geology of Barringer Meteorite Crater, Arizona (a.k.a. Meteor Crater)*. 2nd ed. LPI Contribution 2040. Houston, Texas: Lunar and Planetary Institute. 270 p.

Langenhorst F. 2003. Nanostructures in ultrahigh-pressure metamorphic coesite and diamond: A genetic fingerprint. *Mitteilungen der Österreichischen Mineralogischen Gesellschaft* 148:401–412.

Langenhorst F. and Deutsch A. 2012. Shock metamorphism of minerals. *Elements* 8:31–36.

Losiak A., Wild E. M., Geppert W. D., Huber M. S., Jõeleht A., Kriiska A., Kulkov A., Paavel K., Pirkovic I., Plado J., Steier P., Välja R., Wilk J., Wisniowski T., and Zanetti M. 2016. Dating a small impact crater: An age of Kaali crater (Estonia) based on charcoal emplaced with proximal ejecta. *Meteoritics & Planetary Science* 51:681–695.

Meng E., Xu W. L., Pei F. P., Yang D. B., Wang F., and Zhang X. Z. 2011. Permian bimodal volcanism in the Zhangguangcai Range of eastern Heilongjiang Province, NE China: Zircon U-Pb–Hf isotopes and geochemical evidence. *Journal of Asian Earth Sciences* 41:119–132.

Okuno M., Reynard B., Shimada Y., Syono Y., and Willaime C. 1999. A Raman spectroscopic study of shock-wave densification of vitreous silica. *Physics and Chemistry of Minerals* 26:304–311.

Planetary and Space Science Center. 2021. *The earth impact database*. Fredericton, Canada: Planetary and Space Science Center, University of New Brunswick. http://www.unb.ca/passc

Reimer P. J., Austin W. E. N., Bard E., Bayliss A., Blackwell P. G., Bronk Ramsey C., Butzin M., Cheng H., Edwards R. L., Friedrich M., Grootes P. M., Guilderson T. P., Hajdas I., Heaton T. J., Hogg A. G., Hughen K. A., Kromer B., Manning S. W., Muscheler R., Palmer J. G., Pearson C., Van der Plicht J., Reimer R. W., Richards D. A., Scott E. M., Southon J. R., Turney C. S. M., Wacker L., Adolphi F., Büntgen U., Capano M., Fahrni S. M., Fogtmann-Schulz A., Friedrich R., Köhler P., Kudsk S., Miyake F., Olsen J., Reinig F., Sakamoto M., Sookdeo A., and Talamo S. 2020. The IntCal20 northern hemisphere radiocarbon age calibration curve (0–55 cal kBP). *Radiocarbon* 62:725–757.

Reimold W. U. 2007. The impact crater bandwagon: (Some problems with the terrestrial impact cratering record). *Meteoritics & Planetary Science* 42:1467–1472.

Reimold W. U., Ferrière L., Deutsch A., and Koeberl C. 2014. Impact controversies: Impact recognition criteria and related issues. *Meteoritics & Planetary Science* 49:723–731.

Robertson P. B., Dence M. R., and Vos M. A. 1968. Deformation in rock-forming minerals from Canadian craters. In *Shock metamorphism of natural materials*, edited by French B. M. and Short N. M. Baltimore, Maryland: Mono Book Corp. pp. 433–452.

Schmieder M. and Kring D. A. 2020. Earth's impact events through geologic time: A list of recommended ages for terrestrial impact structures and deposits. *Astrobiology* 20:91–141.

Schultz P. H., Harris R. S., Clemett S. J., Thomas-Keprta K. L., and Zárate M. 2014. Preserved flora and organics in impact melt breccias. *Geology* 42:515–518.

Settle M. 1980. The role of fallback ejecta in the modification of impact craters. *Icarus* 42:1–19.

Song Z., Han Z., Gao L., Geng H., Li X., Meng F., Han M., Zhong W., Li J., Du Q., Yan J., and Liu H. 2018. Permo-Triassic evolution of the southern margin of the Central Asian Orogenic Belt revisited: Insights from Late Permian

igneous suite in the Daheishan Horst, NE China. *Gondwana Research* 56:23–50.

Stähle V., Altherr R., Koch M., and Nasdala L. 2008. Shock induced growth and metastability of stishovite and coesite in lithic clasts from suevite of the Ries impact crater (Germany). *Contributions to Mineralogy and Petrology* 155:457–472.

Stöffler D. and Langenhorst F. 1994. Shock metamorphism of quartz in nature and experiment: I. Basic observation and theory. *Meteoritics* 29:155–181.

Stuiver M., Reimer P. J., and Reimer R. W. 2020. CALIB 8.2 [WWW program]. http://calib.org

Wang Q., Yu Y., Wei J., Zhang L., and Biao S. 2017. Deep constraints mechanism of late Triassic-early Jurassic Yichun-Yanshou granite batholith belt, eastern Heilongjiang. *Mineral Exploration* 8:229–238. (In Chinese)

Wieland F., Reimold W. U., and Gibson R. L. 2006. New observations on shatter cones in the Vredefort impact structure, South Africa, and evaluation of current hypotheses for shatter cone formation. *Meteoritics & Planetary Science* 41:1737–1759.

Windley B. F., Alexeiev D., Xiao W. J., Kröner A., and Badarch G. 2007. Tectonic models for accretion of the Central Asian Orogenic Belt. *Journal of the Geological Society, London* 164:31–47.

Wu F. Y., Sun D. Y., Ge W. C., Zhang Y. B., Grant M. L., Wilde S. A., and Jahn B. M. 2011. Geochronology of the Phanerozoic granitoids in northeastern China. *Journal of Asian Earth Sciences* 41:1–30.

Xu X. M., Trumbore S. E., Zheng S. H., Southon J. R., McDuffee K. E., Luttgen M., and Liu J. C. 2007. Modifying a sealed tube zinc reduction method for preparation of AMS graphite targets: Reducing background and attaining high precision. *Nuclear Instruments and Methods in Physical Research* B259:320–329.

Yin F., Chen M., and Sharp T. 2019. A TEM investigation of formation process of coesite from the Xiuyan impact crater (abstract #6066). Abstracts, 82nd Annual Meeting of the Meteoritical Society. LPI Contribution No. 2157.

Zhou J. B., Wilde S. A., Zhang X. Z., Zhao G. C., Zheng C. Q., Wang Y. J., and Zhang X. H. 2009. The onset of Pacific margin accretion in NE China: Evidence from the Heilongjiang high pressure metamorphic belt. *Tectonophysics* 478:230–246.

Zhu C. Y., Zhao G., Sun M., Eizenhöfer P. R., Han Y., Liu Q., and Liu D. X. 2017. Subduction between the Jiamusi and Songliao blocks: Geochronological and geochemical constraints from granitoids within the Zhangguangcailing orogen, northeastern China. *Lithosphere* 9:515–533.